scientific reports

Check for updates

OPEN

Iron oxyhydroxide as water carrier to the Earth's mantle

Carolina Camarda[1,2], Fernanda Gervasoni[2,3,4]✉, Tiago Jalowitzki[1], Francisco M. C. da Silva[2], Antonio C. Piccino-Neto[2], Paola Ferraz[2], João F.G.A. Oliveira[2], Eduardo X. Miqueles[2], Nathaly L. Archilha[2], Igor Torquato[2], James M. Almeida[5], Daniel G. Cedeño[4,6], Sebastião W. da Silva[7], Reinhardt A. Fuck[1] & Hélio C. N. Tolentino[2]

The discovery of new mineral phases capable of transporting water into the Earth's mantle via subduction zones is essential for understanding the deep Earth water cycle and its influence on mantle dynamics. Recent experimental and computational studies have proposed that certain hydrated oxyhydroxides may remain stable under deep mantle conditions, particularly within cold subducting slabs. Here, we report an advanced synchrotron multi-technique study on a natural complex iron oxyhydroxide mineral preserved within a Juína diamond, which may offer new evidence on water transport via cold subducted slabs and highlights the potential role of iron oxyhydroxides as carriers of volatiles into Earth's interior.

Hydrous minerals within the oceanic lithosphere are the main carrier phases for transporting water into the Earth's mantle at subduction zones (e.g[1].,). Numerous studies suggest the possibility of kilometers of hydration can occur across the oceanic crust and lithosphere, particularly in extensional outer-rise fault zones below the oceanic Moho, which makes the interior of certain subducted slabs even more altered and colder[2] and references therein. While it is well established that a substantial proportion of volatiles, such as OH^-, are recycled into the upper mantle and the transition zone via subduction[1,3], the mechanisms, depths, and mineralogical hosts responsible for water carrier and storage in the mantle remain subjects of ongoing debate.

Water in the upper mantle is primarily stored within the crystal structures of OH-bearing minerals, such as amphibole and mica, or in trace amounts within nominally anhydrous minerals (NAMs) like olivine and pyroxenes[4–6]. In contrast, the mantle transition zone is recognized as a potential water reservoir, as demonstrated by high-pressure experiments on the polymorphs of olivine, wadsleyite and ringwoodite, which have significant OH^- storage capacity[6–9]. This evidence is further supported by investigations of diamond inclusions with the discovery of natural OH-bearing ringwoodite in super-deep diamonds from Juína (Brazil) and Karowe mine (Botswana), both containing a considerable amount of water incorporated into their structure[9,11]. Additional hydrous phases identified in super-deep diamonds include $AlSiO_3(OH)$[12] and ice-VII[13], further corroborating the presence of water in such regions.

Conversely, the knowledge about volatiles and their host minerals in the lower mantle is still based mainly on high-pressure experiments and few findings of volatile-bearing minerals and fluids as inclusions in super-deep diamonds formed at the upper part of the lower mantle[12,14]. These studies suggest that the mineralogy of the lower mantle, as bridgmanite ($(Mg, Fe)(Al, Si)O_3$), davemaoite ($CaSiO_3$) and ferropericlase ($(Mg, Fe)O$), have a deficient water storage capacity[15–17] with the minor phases known as dense hydrous magnesium silicates (DHMSs)[9,18–20] being the main responsible carriers of H_2O in such extreme conditions[3,9,18,19].

Considering that the presence of water in the Earth's mantle can significantly alter its physical and chemical properties, including melting temperature, rheology, phase stability, and the elasticity of constituent minerals[9,18], it is crucial to identify the minerals hosts capable of transporting and storing volatiles that may be stable in the deep mantle and that may act as carriers.

Recent high-pressure experimental studies have proposed that hydrous phases with $CaCl_2$-type structures like δ-AlOOH[12,18,21–23] and α-FeOOH[24–26], as well as dense SiO_2stishovite[23,27], might be stable in cold subducted slabs under extreme conditions and could act as important water carriers into the deep mantle[20]. Particular

[1] Universidade de Brasília, Instituto de Geociências, Programa de Pós-graduação em Geologia, Brasília 70910-900, Brazil. [2]Brazilian Synchrotron Light Laboratory, Brazilian Center for Research in Energy and Materials (LNLS/CNPEM), Campinas 13083-100, Brazil. [3]Centro de Engenharias, Universidade Federal de Pelotas (CEng/UFPel), Pelotas 96010-020, Brazil. [4]Programa de Pós-graduação em Geociências, Universidade Federal do Rio Grande do Sul, Porto Alegre 90040-060, Brazil. [5]Ilum School of Science, Brazilian Center for Research in Energy and Materials (CNPEM), Campinas 13087-548, Brazil. [6]Tectos Analytical Laboratory and Research Center in Geosciences, Dois Irmãos 93950-000, Brazil. [7]Instituto de Física, Universidade de Brasília (IF/UnB), Brasília 70910-900, Brazil. ✉email: fernanda.gervasoni@lnls.br

attention has been given to α-FeOOH (goethite), a ubiquitous hydrated mineral that contains nominally more than 10% water in its structure, and it is found in the layers of oceanic crust and lithosphere[28–31]. These experimental studies have demonstrated that α-FeOOH, if present in cold subducted slabs, may transition to its high-pressure polymorph ε-FeOOH near ~7 GPa and, subsequently decompose into Fe_2O_3 (hematite) and Fe_3O_4 (magnetite) at higher pressures and temperatures (~35–80 GPa; ~875–2475 °C), releasing H_2O and O_2into the deep mantle[24–26].

In this study, we report an advanced synchrotron multi-technique approach that identifies a complex iron oxyhydroxide as an inclusion well encapsulated within a diamond from Juína, Brazil. This iron oxyhydroxide is a mixture of goethite (FeOOH), hematite (Fe_2O_3), and magnetite (Fe_3O_4), which occurs in a diamond that also contains ferropericlase, wüstite, and sulfides. Based on our evidence, we suggest that this iron oxyhydroxide represents a retrograde phase derived from ε-FeOOH, which likely dehydrated and decomposed into iron oxides releasing H_2O and O_2 under deep mantle conditions, rather than being an epigenetic mineral inclusion in the diamond or resulting from hydrous infiltration and alteration of hematite and magnetite. Our observations and hypothesis may provide evidence of complex iron oxyhydroxide phases stable in the Earth's mantle. It also suggests that cold subducted slabs may transport and preserve specific hydrated phases into the deep mantle, potentially releasing hydroxide (OH^-) and oxygen (O^{2-}) at these extreme depths.

Sublithospheric diamond (J1) and its assemblage

This study was conducted at the fourth-generation synchrotron light source SIRIUS[32] in an irregular diamond (J1), translucent, highly reabsorbed, colorless to light-yellow, with dimensions of $3 \times 2 \times 1$ mm^3 (Fig. 1A), collected from the Chapadão Plateau in Juína, Mato Grosso, Brazil. To preserve its integrity, the diamond J1 remained unpolished, making micro-Fourier-transform infrared (FTIR) and micro-Raman spectroscopy analysis challenging. Nonetheless, the diamond was classified as Type IaAB (Fig. S1), with nitrogen aggregated in B centers, and a smaller but still significant amount aggregated in A center[33]. Through Raman spectroscopy,

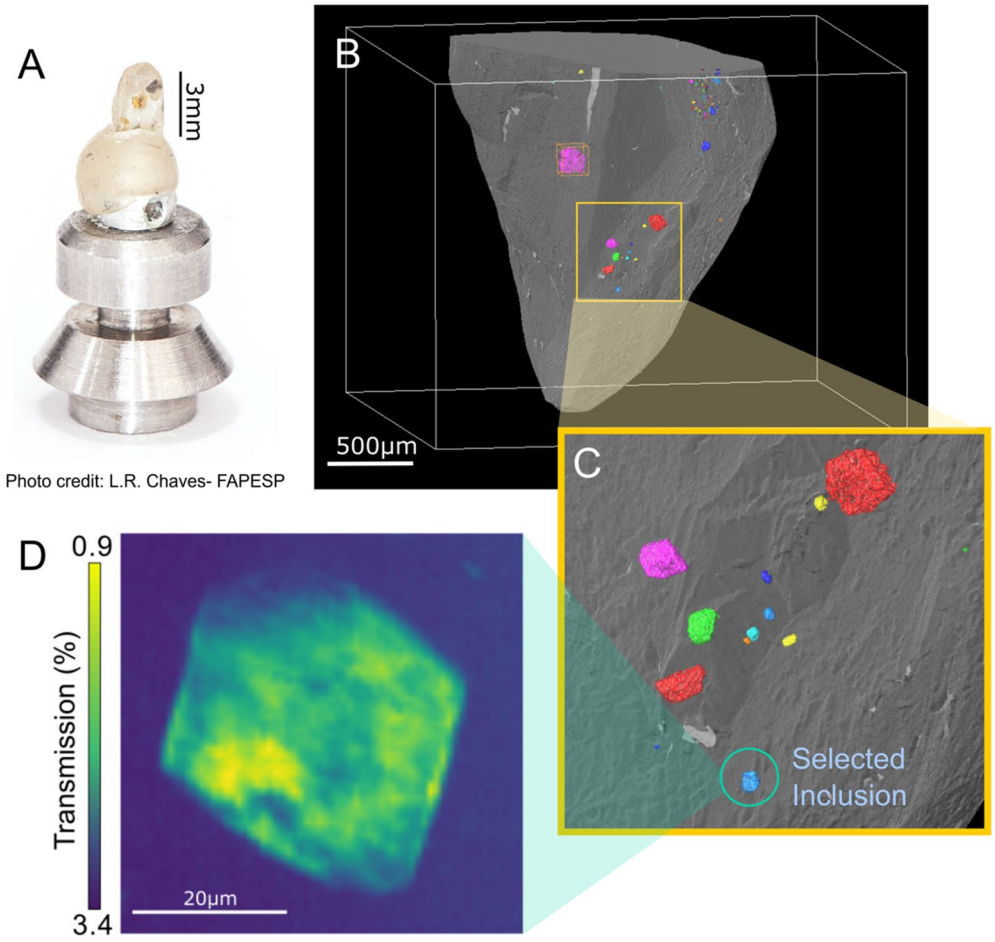

Fig. 1. General views of the diamond J1 and its inclusions. (**A**) Photography of the natural diamond J1 mounted on its holder (photo credit: L.R. Chaves/Pesquisa-FAPESP); (**B**) micro-X-ray Computed Tomography (µ-CT) with a large field of view; (**C**) Zoom of the region of interest; showing the selected inclusion; and (**D**) Scanning Transmission X-ray Microscopy (STXM) with nanometer resolution of the selected inclusion. Note: The false colors applied to (B) and (C) were used to highlight a few inclusions within the diamond matrix. The inclusion indicated in C and shown in D is the Fe oxyhydroxide that is focus of our multi-technique study.

we detected the presence of a potential composite inclusion formed by goethite (FeOOH) and hematite (Fe_2O_3) (Fig. S2). In another region of the diamond, we also detected a Raman peak at 686 cm^{-1}, which is consistent with the presence of ferropericlase (Mg, Fe)O (Fig. S3).

The high-resolution tomography of the J1 diamond (Fig. 1B), obtained via synchrotron radiation micro-computed X-ray tomography (μ-CT), precisely mapped all inclusions in three-dimensional space. Over 100 inclusions were identified and segmented. Among them, synchrotron radiation micro-X-ray diffraction analysis further revealed that the composite inclusion observed in the Raman measurements consists of a Fe oxyhydroxide composed of goethite, hematite, and magnetite, which is the primary focus of this study (Fig. 1C). Additionally, in another region of the diamond, an inclusion of ferropericlase associated with wüstite was identified (Fig. S4), as well as multiple inclusions of sulfides (pentlandite, pyrrhotite, and chalcopyrite). Based on the mineral assemblage observed in the J1 diamond, mainly the ferropericlase inclusions found, we suggest that this diamond formed under pressures corresponding from the ones of sublithospheric diamonds[34], which are considered to have formed at depths from 300 to 1000 km[35].

Fe oxyhydroxide mineral characterization

The Fe oxyhydroxide inclusion studied by scanning transmission X-ray microscopy (STXM) (Fig. 1D) displays dimensions of ≈35 μm. It was verified to be completely encapsulated within the diamond (Fig. S5, Movie S1), with no connection to fractures or exposure to the surface.

The nano X-ray fluorescence computed tomography (n-XFT) (Fig. 2A), reveals that the Fe oxyhydroxide is composed essentially of Fe (~96%) and Ni (~4%), with minor amounts (<1%) of Ti, Cr, and V. The scanned area for each projection in the tomography covers 80 × 80 $μm^2$, with the studied mineral occupying a diameter of ≈35 μm at its center. Consequently, certain elements, such as Ca or Mn, are detected across the scanned area but are not part of the inclusion composition. The elemental distributions show that Fe and Ni exhibit similar density heterogeneities and are highly spatially correlated in the inclusion (Fig. 2B), while Cr, Ti, and V appear as minoritarian contributions (one can see bright spots of Cr outside the inclusion). The n-XFT segmentation focused on the Fe oxyhydroxide (Fig. 2C; Movies S2–S3) reveals regions of varying Fe density, including areas with high, low, and no Fe content. Such nano-tomography also illustrates the inclusion morphology, with the slice highlighting a high-density zone near the bottom (Fig. 2C), and euhedral faces with six sides identified in the crystal basal section. Additionally, very low-density zones devoid of Fe are associated with channels or micropores that are filled with carbon.

Micro-X-ray diffraction (μ-XRD) mapping of the Fe oxyhydroxide inclusion, containing 29 diffraction patterns collected from distinct positions (Fig. S6), reveals a complex and heterogeneous mixture of mineral phases. The inclusion is primarily composed of goethite (α-FeOOH; G) and hematite (Fe_2O_3; H), with subordinate magnetite (Fe_3O_4; M) (Fig. 3). The sum of all diffractograms (Fig. 3A) highlights the presence and indexing of all three phases. Individual diffractograms within the inclusion reveal variable proportions of goethite, hematite, and magnetite as shown by their weighted contributions across the mapped area (Fig. 3B; Fig. S7; Fig. S8). The unit cell parameters and volumes of goethite and hematite (140.32 and 304.65 $Å^3$, respectively), are larger than those of their ambient counterparts by about 1%, indicating structural deviations probably caused by the stress and subsequent retrogression, and the incorporation of Ni into the crystal structure. Spatial variations of these three mineral phases can be observed across the inclusion. Regions with higher Fe density, such as point 19 (Fig. S7), display diffraction patterns dominated by hematite, with sharp reflections indicative of larger crystallite sizes. In

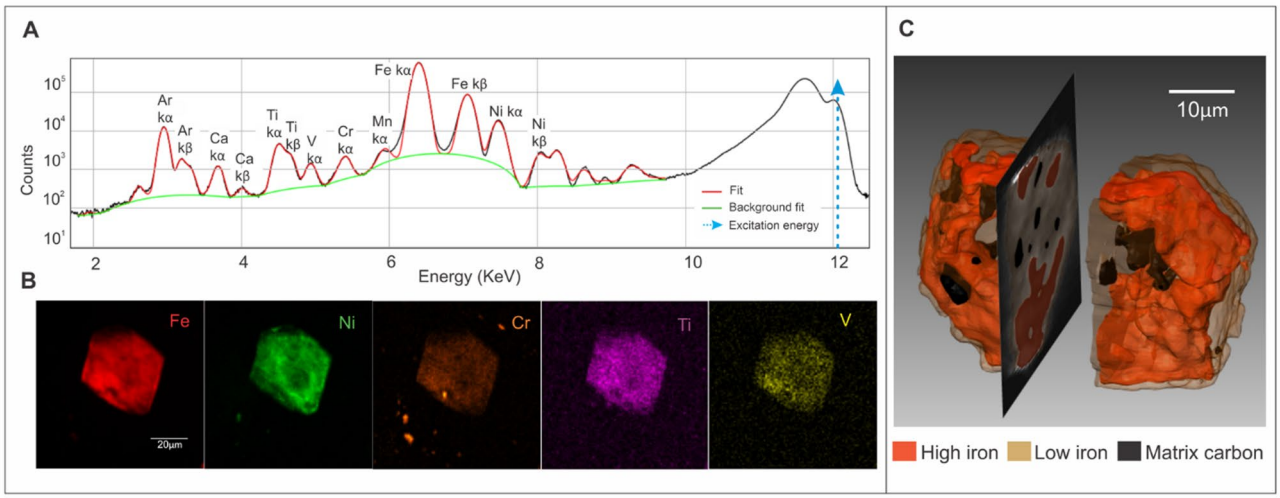

Fig. 2. Nano-X-ray Fluorescence (n-XRF). (**A**) n-XRF spectrum with the identified main element emission lines. Elements such as Ar, Ca, and Mn are from the surroundings and do not belong to the studied mineral; (**B**) 2D n-XRF map formed by the integrated spectra corresponding to the different elements Fe, Ni, Cr, Ti, and V; (**C**) nano-tomography with fluorescence contrast (n-XFCT), segmented in three levels, emphasizing higher and lower amounts of Fe and the channels filled with diamond or carbon matrix.

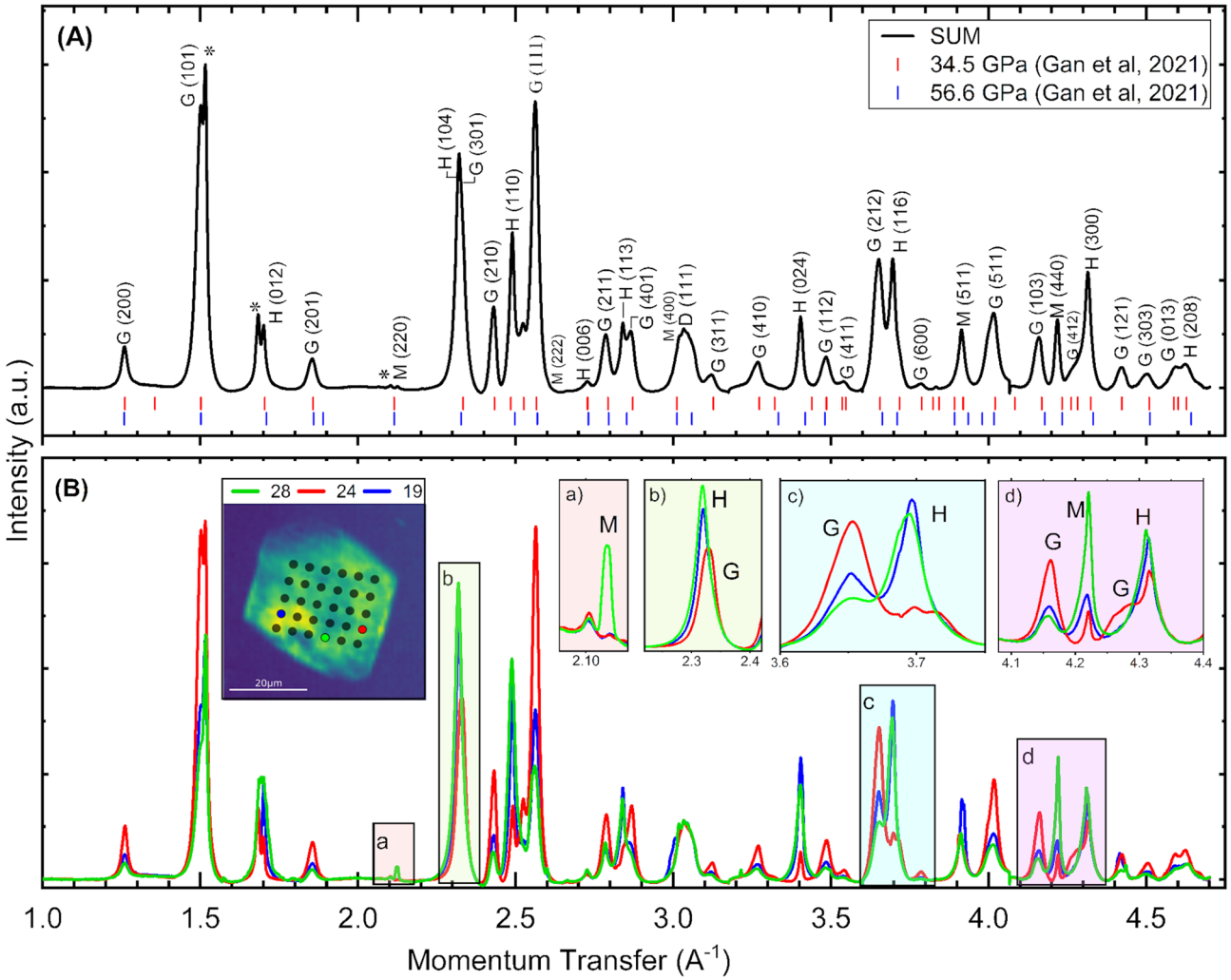

Fig. 3. X-ray diffraction patterns of the Fe oxyhydroxide inclusion. (**A**) Sum of the 29 diffraction patterns across the inclusion, showing phase indexing consistent with goethite (FeOOH), hematite (Fe_2O_3), and magnetite (Fe_3O_4). The diffraction pattern of our inclusion is similar to those obtained in high-pressure shock-recovery experiments at ~35–57 GPa, performed on natural FeOOH and analyzed after shock compression (retrograde phase)[26]. (**B**) Representative diffraction patterns from three selected points illustrate spatial variation in phase composition inside the inclusion. Point 19 (blue dot and line) corresponds to a Fe dense region dominated by hematite; Point 24 (red dot and line) is from a less Fe dense region enriched in goethite; Point 28 (green dot and line) highlights a localized zone containing magnetite within the inclusion. *non-identified phase related to the diamond matrix.

contrast, areas with lower Fe density, such as point 23 (Fig. S7), are enriched in goethite and exhibit intense peaks with well-defined concentric rings, typical of a fine-grained, powder-like texture. Magnetite is in a small central region, as seen in point 28 (Fig. S7). In addition, we performed nanoscale resolution XRD mapping as a 40 × 40 matrix with 400 nm step resolution (Fig. S9). Qualitatively, we observed a detailed diffraction map with the same phase admixture heterogeneities, with goethite more evenly distributed and hematite more concentrated in the denser regions, showing a few crystallites with higher intense reflections.

Overall, μ-XRD mapping demonstrates that goethite and hematite are pervasive throughout the inclusion, while magnetite appears restricted to its core (Fig. S8A-E). This spatial distribution of the three phases along the inclusion, with no fractures connecting it to other mineral inclusions or to the diamond, suggests that this Fe oxyhydroxide may have been captured by the host diamond in a transitional state, during a progressive decomposition and transformation from one phase to the others, which might have occurred in the deep mantle.

The dihydroxylation of goethite to hematite is a well-known oxidation reaction that typically occurs during diagenesis[36]. The reverse reaction is also commonly observed at the surface in sediments and soils, with hydration of Fe oxides and being transformed into goethite. However, the simultaneous occurrence of goethite, hematite, and magnetite within a single inclusion is unusual in natural systems, as it requires specific physical parameters and distinct redox conditions to stabilize each phase together in the same inclusion. The reduction of hematite to magnetite, or directly the transformation of goethite to magnetite, or even the transition

from goethite to hematite and magnetite, is rare under natural conditions and generally requires elevated temperatures and the presence of organic carbon[37]. On the other hand, the transition from α-FeOOH to its high-pressure polymorph ε-FeOOH, followed by decomposition into Fe oxides, such as hematite and magnetite polymorphs, with the release of H_2O and O_2, has been observed under high-pressure and high-temperature experimental conditions representative of the deep mantle[24–26,38,39]. Notably, our XRD patterns of the complex Fe oxyhydroxide inclusion shows the presence of an assembly that has also been found by high-pressure shock-recovery experiments[26] (Fig. 3A). It was observed that pristine α-FeOOH first transforms into ε-FeOOH, and with increasing shock wave pressures and temperature (~35–57 GPa; 877–1827 °C), it partially decomposes into other Fe-oxides[26]. Their diffraction patterns, obtained with the post-shock samples, represent retrograde phases (goethite, hematite, and magnetite) that crystallized upon decompression and cooling, reflecting the products of high-pressure ε-FeOOH breakdown. These pressures and temperatures represent lower mantle conditions at approximately ~900 to 1,250 km depths[26]. If we propose that the complex Fe oxyhydroxide pathway observed in our study is analogous to that seen in shock-wave experiments, we could infer that the Juína diamond and its inclusion experienced similar conditions, potentially reaching the mantle transition zone and lower mantle. However, it is important to emphasize that this remains a hypothesis. Shock-wave compression follows a Hugoniot P-T path, and the subsequent release is approximately isentropic, which differs from static compression experiments such as diamond anvil cells (DAC) and from the pressure and temperature conditions expected in the deep mantle.

Oxidation state and coordination environment of Fe and Ni atoms

Micro-X-ray absorption near-edge structure (μ-XANES) spectroscopy mapping was conducted on the Fe K-edge at multiple locations (Fig. S10) in the Fe oxyhydroxide inclusion, revealing distinct Fe oxides mixed-phases (Fig. 4A). The analysis identified two principal components with almost equivalent weights but heterogeneously distributed (Fig. S11): the component 1 resembled goethite but with a shifted absorption edge to lower energies (≈ −1.6eV), while component 2 contained spectral features closer to hematite. Compatible with our XRD results, component 2 is prominent around the Fe denser region (Fig. S11B). Both components showed smooth spectral features indicative of a larger disorder than the standard mineral phases (Fig. S11C), consistent with more defects caused by the high-stress conditions in the deep mantle where the inclusion was probably formed, as we are suggesting in this study. The edge shift to lower energy may indicate a less oxidized iron state or local structural defects. Our preliminary simulations (Fig. S12) show that introducing oxygen vacancies and relaxing the structure creates a density of states at lower energies close to the edge. This effect is particularly evident in the case of goethite (Fig. S12A). A similar shift in the electronic structure of goethite under pressure, both during and after laser heating experiments, has been previously observed[40], and has been attributed to the formation of Fe^{2+} oxidation states.

To get into the Fe oxidation state, we investigated XANES pre-edge by fitting and identifying the electronic transitions (Fig. S13) and then calculating the centroid for each spectrum (Table S1). The established centroid-position diagram (Fig. S14)[41], points to an inclusion as a mixture of Fe^{3+} and Fe^{2+} in octahedral coordination. This finding contrasts with typical minerals at ambient pressures, where Fe^{2+} in magnetite occupies the tetrahedral coordination site, and hematite or goethite lacks Fe^{2+} in its structure. The Fe^{2+} oxidation state, about 10 to 15%, indicates possible defective sites, like oxygen vacancies or OH^- replacing O^{2-}, which could occur in any of the mineral phases that compose our inclusion. We hypothesize that Fe^{2+} may either replace Fe^{3+} in the FeOOH and Fe_2O_3 structures, with local chemical replacement of O^{2-} by OH^-, or accommodate itself within crystal defects or vacancies. These mechanisms are supported by our Fe K-edge μ-XANES results, which reveal structural distortions and mixed valence states, and by the unit cell parameters and volumes increase for goethite and hematite.

Considering that the Fe oxyhydroxide inclusion absorbs up to 4% Ni in its structure, we also conducted μ-XANES mapping at the Ni K-edge (Fig. 4B). The Ni K-edge exhibited spectral features corresponding to the pure Ni^{2+} oxidation state centered in an octahedron like $NiO_2(OH)_4$, a distinctive coordination when Ni^{2+} replaces Fe^{3+} in natural goethite[42] or other oxides[43]. In contrast to the spectral heterogeneities observed for Fe, the Ni oxyhydroxide distribution is homogeneous, implying a widespread substitution in the defective goethite or hematite phases. The Ni^{2+} replacement for Fe^{3+} in octahedral sites requires a new charge balance, leading to the local substitution of O^{2-} by OH^-, converting $FeO_3(OH)_3$ into $NiO_2(OH)_4$octahedra[42].

Fe oxyhydroxide and its polymorphs decomposition into the Earth's mantle

The stability of goethite polymorphs under high pressure and temperature conditions has been investigated through both experimental studies and computational modeling. At pressures of approximately 5–7 GPa and temperatures near 200 °C, α-FeOOH transforms into its high-pressure polymorph ε-FeOOH[44–46]. This phase exhibits a crystal structure that may remain stable at mid-lower mantle depths, within the pressure range of ~35–70 GPa[26,39]. Some experimental studies further suggest that, under deep lower mantle conditions (~80 GPa), ε-FeOOH is still stable and can transform into an even higher-pressure phase, known as the pyrite-type FeO_2H_x("py-phase"; where $x \leq 1$; space group $Pa\bar{3}$) that may be stable until depths representative of the core-mantle boundary[4,5,7–9,9–49].

Goethite (α-FeOOH) is often overlooked in diamonds[50–53], because it is a ubiquitous mineral present in soils and sediments, and therefore is usually considered as an epigenetic phase formed either by precipitation into diamond cracks or by hydrous reaction of Fe oxides resulting from fluid infiltration along diamond fractures. However, this is not the case of the J1 diamond studied here, which hosts a well-encapsulated Fe oxyhydroxide inclusion observed by micro and nano-tomography, along with other inclusions such as ferropericlase, wüstite, and sulfides, suggesting an origin in the deep mantle. This Fe oxyhydroxide is a heterogeneous mixture of goethite, hematite, and magnetite. Rather than interpreting the studied inclusion as epigenetic, we consider the

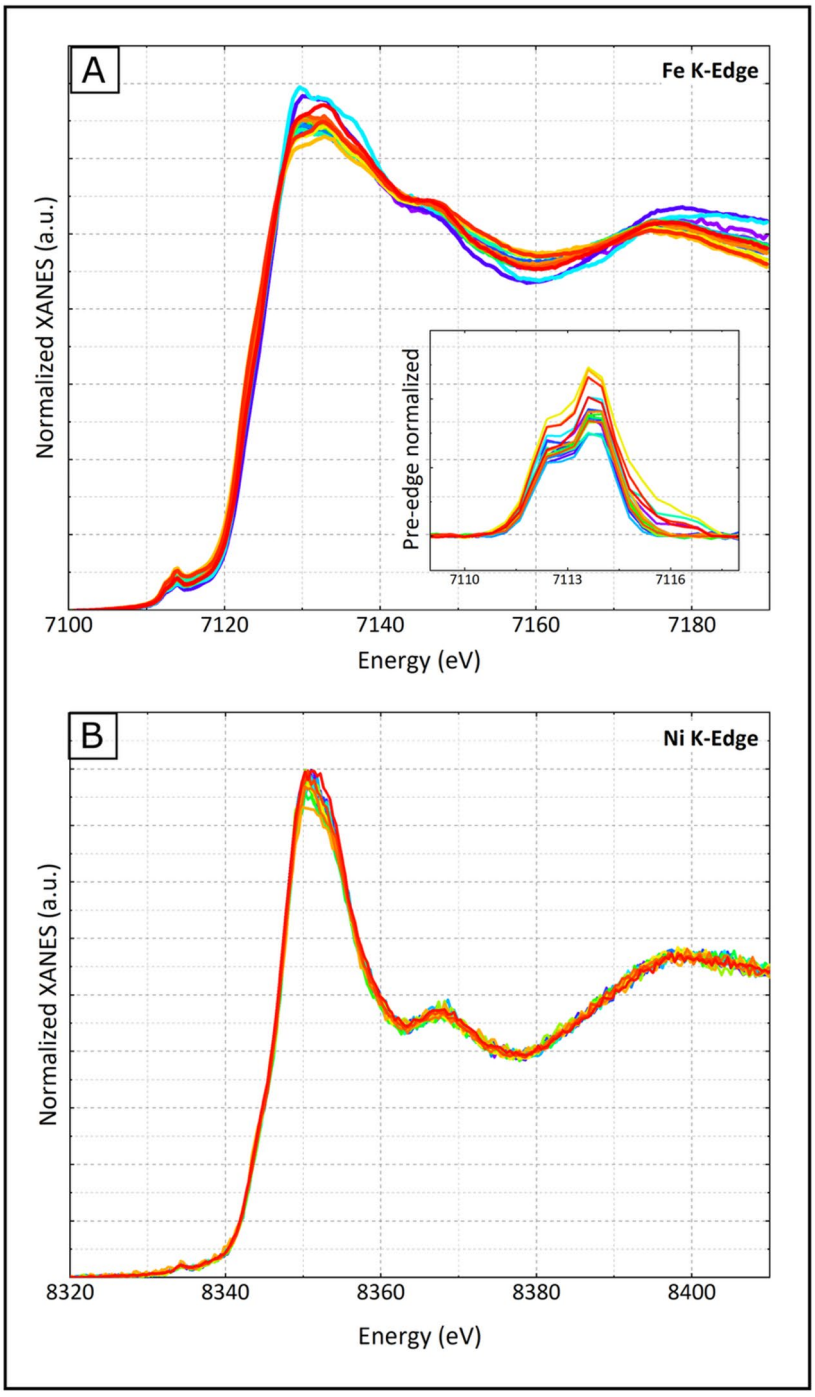

Fig. 4. (**A**) μ-XANES spectroscopy at the Fe K-edge and (insert) the normalized pre-edge showing a non-homogenous spectral shape depending on the location in the inclusion. The color bar indicates the 18 mapped points according to the transmission image (Fig. S10A). (**B**) μ-XANES spectroscopy at the Ni K-edge exhibiting the same pattern in all mapped points, as shown in the transmission image, totalizing 16 points (Fig. S10B).

phase assemblage within the Fe oxyhydroxide inclusion as a record of retrograde transformation, reflecting the breakdown of ε-FeOOH into Fe_2O_3 and Fe_3O_4. Based on the mineralogy of the J1 diamond and on experimental studies, we suggest that this transformation likely occurred under pressure and temperature conditions corresponding to the deep mantle (Fig. 5, Fig S15).

The μ-XRD mapping of the Fe oxyhydroxide inclusion match with retrograde phases identified in shock-recovery experiments, in which ε-goethite decomposed into hematite and magnetite under pressure and temperature conditions comparable to those expected in cold subducted slabs reaching the deep mantle (~ 35–57 GPa; 877–2470 °C)[26] (Fig. S15). Making an analogy between the complex Fe oxyhydroxide in our study and

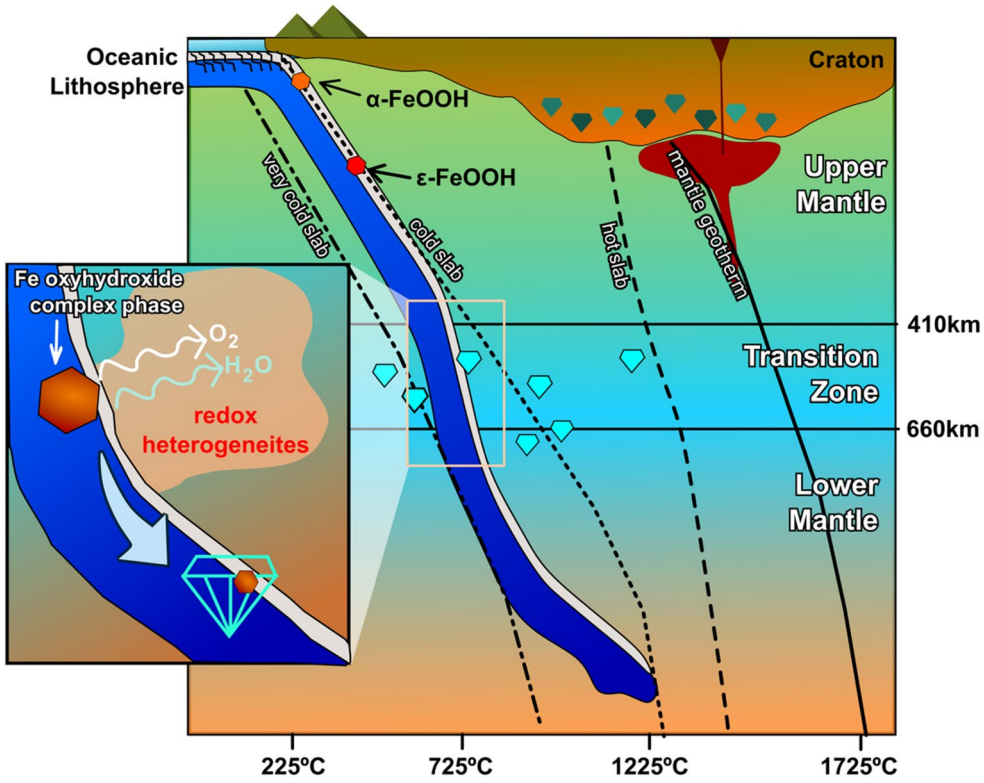

Fig. 5. Schematic cross-section showing a cold subducted slab descending through the mantle transition zone into the deep mantle. The cold, very cold slab and hot geotherms are represented by dashed lines[54,55]. The mantle geotherm is represented by the black line[57]. The α-FeOOH found in the oceanic crust or lithosphere transforms into its high-pressure polymorph, ε-FeOOH at ~ 230 km depth (~ 7 GPa)[26,39]. As the slab descends to deeper regions, the ε-FeOOH begins to break down into Fe_2O_3 and Fe_3O_4, releasing volatiles into the surrounding rocks (inset figure). This transformation may form localized redox heterogeneities in the mantle. The phase transformation is incomplete, forming a heterogeneous Fe oxyhydroxide assemblage in the crystal (inset), which is then trapped in a diamond, potentially crystallized from fluids and melts released by the slab (inset figure)[26,39].

those tested under high-pressure experiments[24,26,38,39,44], we may suggest that the studied inclusion experienced comparable pressure and temperature conditions, potentially corresponding to the deep mantle. In addition to the μ-XRD data, the μ-XANES spectroscopy reveals a disordered structure distinct from phases typically stable at ambient pressure, suggesting that the mineral phases comprising the complex Fe oxyhydroxide likely formed under intense stress associated with extreme mantle conditions, supporting our interpretation.

Therefore, based on our hypothesis and corroborated by experimental results[24,25,26,39,54,55], we propose a model in which the complex Fe oxyhydroxide was originally formed as α-FeOOH within a cold subducted slab, and subsequently underwent a phase transition to ε-FeOOH at ~ 7 GPa (Fig. 5). This phase remained stable until the slab reached the deep upper mantle, transition zone and the uppermost part of the lower mantle, when the ε-FeOOH began to partially decompose into Fe-oxide phases (Fe_2O_3 and Fe_3O_4), releasing H_2O and O_2 (Fig. 5). Under these conditions, the heterogeneous Fe oxyhydroxide inclusion was encapsulated within a diamond, which either pre-existed in the mantle or crystallized simultaneously from melts or fluids derived from the same cold subducted slab that brought the FeOOH (Fig. 5)[3,56].

Possible implications of H_2O and O_2 released from FeOOH decomposition into the Earth's deep mantle

Mineral inclusions in super-deep diamonds, as well as helium isotopes, have provided evidence that the mantle transition zone and the upper part of the lower mantle interacted with fluids and melts from subducting sla bs[10,11,56,58–60]. Seismic tomography data and observations of focal mechanisms and local earthquakes suggest the accumulation of slabs in the transition zone at 660 km depth[2] and references therein), with the possibility of some slabs descending into the lower mantle[61–66]. Thus, our hypothesis based on the FeOOH transitioning to Fe oxides and realizing H_2O and O_2 into the deep mantle implies that cold subducted slabs can reach extreme conditions not only with dense hydrous magnesium silicates (DHMS) as stable hydrous minerals[2,3,9,17,20,22], but also Fe oxyhydroxides (Fig. 5, Fig. S15).

The decomposition of ε-FeOOH observed in high-pressure experiments[26,39] may follow the suggested reactions[26]:

$$2FeOOH \rightarrow Fe_2O_3 + H_2O \quad (1)$$

$$12FeOOH \rightarrow 4Fe_3O_4 + 6H_2O + O_2 \quad (2)$$

$$6Fe_2O_3 \rightarrow 4Fe_3O_4 + O_2 \quad (3)$$

These reactions demonstrate a complex redox condition along with the formation of hematite and magnetite, and the release of H_2O and O_2. In this way, the natural occurrence of ε-FeOOH transitioning to Fe oxides with consequent release of volatiles, highlights the significance of Fe oxyhydroxides as possible carriers of water into the deep mantle, and may introduce a new perspective about our understanding of the deep Earth and its oxidation state. The oxygen fugacity (fO_2) of the deep mantle should be relatively low, based mainly on its major mineralogical constituents[15,67]. However, the introduction of relicts of cold slabs into the uppermost part of the lower mantle, for instance, can disrupt this relatively homogeneous redox environment. In particular, our hypothesis suggests that the decomposition of oxyhydroxides releasing OH^- and O^{2-} at these depths, may form localized chemical heterogeneities (Fig. 5). These processes could modify the redox state of the surrounding mantle where the cold subducted slabs may reach, potentially creating highly complex redox microenvironments. The liberated H_2O and O_2 from the Fe oxyhydroxide decomposition can either be incorporated into the crystal structures of other complex mantle phases or trigger redox reactions with adjacent minerals, further modifying the local chemical and physical properties of the deep mantle.

Methods

Micro raman spectroscopy

Due to the challenges of obtaining good spectra in a highly reabsorbed diamond with an irregular surface (non-polished), only three mineral phases could be detected: ferropericlase, goethite, and hematite. The Raman spectra of the detected inclusions are slightly shifted. The μ-Raman spectroscopy analyses were performed at the Brazilian Nanotechnology National Laboratory (LNNano/CNPEM) using a Horiba Xplora Scientific Plus spectrometer. The analyses were repeated three times on different days, using a red laser (638 nm) to verify the occurrence of mineral phases. The analysis took 5 s with 10 accumulations, range between 100 and 1199 cm^{-1}, objective = 50 x(LWD), grating = 1200 (750 nm), filter = 25%, slit = 50 μm, and hole = 100 μm. The data processing was performed using the KnowItall (trial version), Wire 4.4, and OriginPro software.

Micro-fourier transform infrared (FTIR)

Micro-FTIR spectroscopy was conducted at the IMBUIA beamline, at an off-line source, of the LNLS using an Agilent Cary 600 FTIR spectrometer equipped with XT-KBr beam splitters and an MCT-A detector. The objective was to determine nitrogen concentrations and aggregation states in the diamond samples. Some challenges were encountered in obtaining a good transmission and clear spectra, particularly in the spectral region critical for classifying nitrogen aggregation states, probably due to the choice of using the rough diamond without polished planes. Transmission spectra were collected in the range of 4000–500 cm^{-1}, with a spectral resolution of 8 cm^{-1}, and averaged over 512 scans. Background spectra (also 512 scans) were acquired prior to each analysis. Spectral deconvolution was performed using the DiaMap software[7071]. The diamond analyzed in this study is classified as Type IaB. The FTIR spectrum is provided in Fig. S1. Nitrogen aggregation is mostly in the B-center, with some amount in A-center, classifying this diamond as Type IaAB[33].

Multiple synchrotron radiation techniques – SIRIUS (LNLS)

Our findings have been uncovered thanks to the high-brilliant 4th-generation synchrotron light source at the Brazilian Synchrotron Light Laboratory (LNLS) - SIRIUS, which enabled the use of multiple beamlines and advanced analytical techniques, as well as the screening of numerous pristine diamond samples. To preserve the natural morphology and all enclosed inclusions, all analyses were conducted on an unpolished diamond sample. The diamond was donated from Mr. Romeu Veronese, and it was collected at the Chapadão Plateau, Juína, Mato Grosso, Brazil.

Micro-X-ray computed tomography (μ-CT)

The micro-X-ray computed tomography (μ-CT) was performed during the scientific commissioning phase of the MOGNO beamline[72] (LNLS-SIRIUS). The beam used for the analysis had an energy of 22 keV with an effective pixel size of 1.46 μm. Data reconstruction was carried out by the Scientific Computing Group (GCC) at SIRIUS, using an in-house implementation of the Feldkamp–David–Kress (FDK) method[73], while the 3D segmentation of the tomography was performed using AvizoS software. The high-resolution 3D map of the J1 diamond, obtained through this micro-computed tomography (μ-CT), accurately identified more than 100 inclusions within the sample. Additionally, the map located all inclusions in space, as well as some fractures in the diamond. The oxyhydroxide inclusion selected for this study has a diameter of 35 μm and is fully encapsulated within the diamond.

Micro X-ray diffraction (μ-XRD)

The micro-X-ray diffraction data acquisition was performed at the EMA beamline[74] (LNLS-SIRIUS). The incident beam size was 5 μm in diameter, with an energy of 12,658 eV. The calibration standard used was $LaB_6$with a wavelength of 0.9795 Å. A point mapping was carried out on the main inclusion, consisting of 30 diffraction points arranged in a 6×5 matrix with a 5 μm spacing between points. Each point took an average of 2 min for acquisition with an angular range from 0° to 44°. The data were subsequently processed using OriginPro and Dioptas[75].

Nano X-ray diffraction

The nano-X-ray diffraction data acquisition was performed at the CARNAÚBA beamline[76] to certify our diffraction data collected of micro-XRD at the EMA beamline. The incident beam size was 400×200 nm^2, with an energy of 10,000 eV. The calibration standard used was LaB_6 with a wavelength of 1.240 Å. A full mapping was carried out on the inclusion, consisting of 1681 diffraction points arranged in a 41×41 matrix with a 1 μm spacing between points. Each point took an average of 5 s for acquisition. In this case, the angular range was limited from 11.5° to 32.7°. The data were subsequently processed using a Python code.

Nano-X-ray fluorescence (n-XRF)

The nano-X-ray fluorescence (n-XRF) mapping was conducted at the CARNAÚBA beamline[76] (LNLS-SIRIUS) with the aim of discovering the compositional variation within the inclusion. n-XRF maps were measured, encompassing the entire inclusion and a specific region within the inclusion. Both maps were performed with an energy of 12 keV, with an acquisition time of 172 s (7.5 ms/pixel), in a scan area of 80×80 and 10×10 μm^2, with pixel sizes of 800 and 100 nm, respectively. The XRF curve calibration was performed using the PyMca software, yielding an evaluation of the relative element content. Nano-X-ray Fluorescence (n-XRF) maps were acquired simultaneously with the STXM measurements. The 2D maps were collected at several projections to produce nano-computed tomography (n-CT) together with nano X-ray fluorescence tomography (n-XFT) contrasts (see below).

Nano-X-ray tomography

The nanometer-sized beam (< 500 nm) of CARNAÚBA beamline[76] extends this technique to the nanoscale with high resolution, and its high flux allows that a wide range of elements be mapped, providing 3D elemental imaging. To perform tomography measurements, it is necessary to pre-align the sample, centering it at different rotation angles (RY), so as an internal code of the beamline can be processed to provide a set of parameters for proper tomography execution. The alignment of the inclusion precedes the tomography experiment and was done with an energy of 12 keV, a scanned area of 100×100 μm^2 with a 5 μm step. The experiment acquisition was carried out at the same energy of 12 keV, a scan area of 80×80 μm^{2}with a 0.8 μm step and a 2° angular increment, totaling 9 h of experiment (2 hours of alignment + 7 h of acquisition). For the fluorescence data, the reconstruction was carried out by the Scientific Computing Group (GCC) at SIRIUS through a modified version of the Chang's method[77] using as inputs the μ-Tomography reconstruction to account for diamond-related self-absorption effects that are not in the field of view (FOV) region, as well as the nano tomographic reconstruction for the absorption effects within the FOV. For both tomography and fluorescence measurements, the final reconstructed data object has a voxel size of $0.8 \times 0.8 \times 0.8$ μm^3 and a total region of $80 \times 80 \times 80$ μm^3, with a total of 101 slices for segmentation, which was done using AvizoS software.

X-ray absorption near edge structure (XANES) spectroscopy

Absorption spectroscopy was conducted on CARNAÚBA beamline[76] and focused only on the region near the absorption edge. XANES data were acquired in step scan mode. Before starting the measurements, standards of Fe-metal (Fe foil), Fe_2O_3, Fe_3O_4, FeO, and Ni-metal (Ni foil) were used, with scans of 100 eV around their respective K-edge absorption edges. Two XANES maps were performed in step scan mode at two different K-edges: iron and nickel. The acquisition time per point was 0.5 s, and the energy step was 0.4 eV, for each map. The Fe K-edge map has 25 (5×5 matrix) points (18 effective), an energy variation from 7100 to 7200 eV, and a total acquisition time of 125 min. The Ni K-edge map has 16 (4×4 matrix) points, an energy variation from 8320 to 8420 eV, and a total acquisition time of 80 min.

To identify the components of the XANES spectrum, Multivariate Curve Resolution with Alternating Least Squares (MCR-ALS) were employed. The software used for the analysis was CORAL (in house software), developed by the QUATI beamline.

The XANES spectroscopy simulations were performed using available CIF files from goethite and hematite, introducing the defects manually, and applying the Quantum Espresso and FDMNES packages. The structural relaxations were performed with the Quantum Espresso package[78,79] using the solid-state pseudopotential (SSSP)[80]. The wavefunction cutoff was 90 Ry, and the charge density cutoff was 1080 Ry. The exchange-correlation functional employed was the Perdew-Burke-Ernzerhof (PBE)[81]. For the XANES spectra simulations, the FDMNES software was used[82–84], the calculations were self-consistent with a cluster radius of 7.0 Angstroms, with the multiple scattering mode, where a muffin-tin potential is employed.

Data availability

"All data are available in the main text or the supplementary information."

Received: 10 February 2026; Accepted: 27 March 2026
Published online: 11 May 2026

References

1. Faccenda, M. Water in the slab: A trilogy. *Tectonophysics* **614**, 1–30 (2014).
2. Shirey, S. B., Wagner, L. S., Walter, M. J., Pearson, D. G. & van Keken, P. E. Slab transport of fluids to deep focus earthquake depths—thermal modeling constraints and evidence from diamonds. *AGU Adv.* https://doi.org/10.1029/2020AV000304 (2021).
3. Nestola, F. & Smyth, J. R. Diamonds and water in the deep Earth: A new scenario. *Int. Geol. Rev.* **58**, 263–276 (2016).
4. Schmidt, M. W. & Poli, S. Devolatilization During Subduction. In *Treatise on Geochemistry* second edition, Vol. vol. 4 669–701 (Elsevier Inc., 2013).

5. Grützner, T., Klemme, S., Rohrbach, A., Gervasoni, F. & Berndt, J. The role of F-clinohumite in volatile recycling processes in subduction zones. *Geology* **45**, 443–446 (2017).
6. Carvalho, L. D. V. et al. Dense hydrated Mg-silicates in diamond: Implications for transport of H2O into the mantle. *Sci. Adv.* **10**, eadl4306. https://doi.org/10.1126/sciadv.adl4306 (2024).
7. Kohlstedt, D. L., Keppler, H. & Rubie, D. C. Solubility of water in the α, β and γ phases of (Mg,Fe)2 SiO4. *Contrib. Mineral. Petrol.* **123**, 345–357 (1996).
8. Smyth, J. R. et al. Crystal structure of monoclinic hydrous wadsleyite [β-(Mg,Fe)2 SiO4]. *Am. Mineral.* **82**(3–4), 270–275 (1997).
9. Hirschmann, M. M. Water, melting, and the deep Earth H2O cycle. *Annu. Rev. Earth Planet. Sci.* **34**, 629–653 (2006).
10. Pearson, D. G. et al. Hydrous mantle transition zone indicated by ringwoodite included within diamond. *Nature* **507**, 221–224 (2014).
11. Gu, T. et al. Hydrous peridotitic fragments of Earth's mantle 660 km discontinuity sampled by a diamond. *Nat. Geosci.* **15**, 950–954 (2022).
12. Wirth, R., Vollmer, C., Brenker, F., Matsyuk, S. & Kaminsky, F. Inclusions of nanocrystalline hydrous aluminium silicate "Phase Egg" in superdeep diamonds from Juina (Mato Grosso State, Brazil). *Earth Planet. Sci. Lett.* https://doi.org/10.1016/j.epsl.2007.04.041 (2007).
13. Tschauner, O. et al. Ice-VII inclusions in diamonds: Evidence for aqueous fluid in Earth's deep mantle. *Science* **359**, 1136–1139. https://doi.org/10.1126/science.aao3030 (2018).
14. Smith, E. M. et al. Blue boron-bearing diamonds from Earth's lower mantle. *Nature* **560**, 84–87. https://doi.org/10.1038/s41586-018-0334-5 (2018).
15. Murakami, M., Hirose, K., Yurimoto, H., Nakashima, S. & Takafuji, N. Water in Earth's lower mantle. *Science* **295**, 1885–1887. https://doi.org/10.1126/science.1065998 (2002).
16. Litasov, K. et al. Water solubility in Mg-perovskites and water storage capacity in the lower mantle. *Earth Planet. Sci. Lett.* **211**, 189–203. https://doi.org/10.1016/s0012-821x(03)00200-0 (2003).
17. Bolfan-Casanova, N. Water in the Earth's mantle. *Mineral. Mag.* **69**, 229–258. https://doi.org/10.1180/0026461056930248 (2005).
18. Tsuchiya, J. & Thompson, E. C. The role of hydrogen bonds in hydrous minerals stable at lower mantle pressure conditions. *Prog. Earth Planet. Sci.* **9**, 63. https://doi.org/10.1186/s40645-022-00521-3 (2022).
19. Ringwood, A. E. & Major, A. High-pressure reconnaissance investigations in the system Mg2SiO4-MgO-H2O. *Earth Planet. Sci. Lett.* **2**, 130–133. https://doi.org/10.1016/0012-821X(67)90114-8 (1967).
20. Walter, M. J. Water transport to the core–mantle boundary. *National Science Review* https://doi.org/10.1093/nsr/nwab007 (2021).
21. Pamato, M. et al. Lower-mantle water reservoir implied by the extreme stability of a hydrous aluminosilicate. *Nat. Geosci.* **8**, 75–79. https://doi.org/10.1038/ngeo2306 (2015).
22. Walter, M. J. et al. The stability of hydrous silicates in Earth's lower mantle: Experimental constraints from the systems MgO–SiO2–H2O and MgO–Al2O3–SiO2–H2O. *Chem. Geol.* **418**, 16–29. https://doi.org/10.1016/j.chemgeo.2015.05.001 (2015).
23. Nisr, C. et al. Large H2O solubility in dense silica and its implications for the interiors of water-rich planets. *Proc. Natl. Acad. Sci. U. S. A.* **117**(18), 9747–97. https://doi.org/10.1073/pnas.1917448117 (2020).
24. Hu, Q. et al. FeO2 and FeOOH under deep lower-mantle conditions and Earth's oxygen-hydrogen cycles. *Nature* **534**, 241–244 (2016).
25. Nishi, M., Kuwayama, Y., Tsuchiya, J. & Tsuchiya, T. The pyrite-type high-pressure form of FeOOH. *Nature* **547**, 205–208 (2017).
26. Gan, B. et al. Partial Deoxygenation and Dehydration of Ferric Oxyhydroxide in Earth's Subducting Slabs. *Geophys. Res. Lett.* **48**, e2021GL094446. https://doi.org/10.1029/2021GL094446 (2021).
27. Lin, Y., Hu, Q., Meng, Y., Walter, M. & Mao, H. Evidence for the stability of ultrahydrous stishovite in Earth's lower mantle. *Proc. Natl. Acad. Sci. U. S. A.* **117**(1), 184–189. https://doi.org/10.1073/pnas.1914295117 (2020).
28. Drodt, M., Trautwein, A., König, I., Suess, E. & Bender Koch, C. Mössbauer spectroscopic studies on the iron forms of deep-sea sediments. *Phys. Chem. Miner.* **24**, 281–293 (1997).
29. Marescotti, P., Vanko, D. A. & Cabella, R. From oxidizing to reducing alteration: Mineralogical variations in pillow basalts from the east flank, Juan de Fuca Ridge. In Proc. Ocean Drill. Program Sci. Results 168, 119–140. https://doi.org/10.2973/odp.proc.sr.168.010.2000 (2000).
30. Charpentier, D., Buatier, M. D., Jacquot, E., Gaudin, A. & Wheat, C. G. Conditions and mechanism for the formation of iron-rich montmorillonite in deep sea sediments (Costa Rica margin): Coupling high resolution mineralogical characterization and geochemical modeling. *Geochim. Cosmochim. Acta* **75**(6), 1397–1410. https://doi.org/10.1016/j.gca.2010.11.026 (2011).
31. Homoky, W. B. et al. Iron and manganese diagenesis in deep sea volcanogenic sediments and the origins of pore water colloids. *Geochim. Cosmochim. Acta* **75**(17), 5032–5048. https://doi.org/10.1016/j.gca.2011.06.019 (2011).
32. Liu, L., Neuenschwander, R. T. & Rodrigues, A. R. D. Synchrotron radiation sources in Brazil. *Philos. Trans. R. Soc. Lond. A Math. Phys. Eng. Sci.* **377**, 20180235. https://doi.org/10.1098/rsta.2018.0235 (2019).
33. Day, M. C., Pamato, M. G., Novella, D. & Nestola, F. Imperfections in natural diamond: The key to understanding diamond genesis and the mantle. *Riv. Nuovo Cimento* **46**, 381–471. https://doi.org/10.1007/s40766-023-00045-6 (2023).
34. Kaminsky, F. V., Zedgenizov, D. A., Sevastyanov, V. S. & Kuznetsova, O. V. Distinct groups of low- and high-Fe ferropericlase inclusions in super-deep diamonds: An example from the Juina Area, Brazil. *Minerals* **13**(9), 1217. https://doi.org/10.3390/min13091217 (2023).
35. Nestola, F. et al. CaSiO3 perovskite in diamond indicates the recycling of oceanic crust into the lower mantle. *Nature* **555**, 237–241 (2018).
36. Landers, M. & Gilkes, R. J. Dehydroxylation and dissolution of nickeliferous goethite in New Caledonian lateritic Ni ore. *Appl. Clay Sci.* **35**(3–4), 167–172 (2007).
37. Till, J. L. & Nowaczyk, N. Authigenic magnetite formation from goethite and hematite and chemical remanent magnetization acquisition. *Geophys. J. Int.* **213**(3), 1818–1831. https://doi.org/10.1093/gji/ggy083 (2018).
38. Hu, Q. et al. Dehydrogenation of goethite in Earth's deep lower mantle. *Proc. Natl. Acad. Sci. U. S. A.* **114**(7), 1498–1501. https://doi.org/10.1073/pnas.1620644114 (2017).
39. Koemets, E. et al. Chemical Stability of FeOOH at High Pressure and Temperature, and Oxygen Recycling in Early Earth History**. *Eur. J. Inorg. Chem.* **2021**, 3048–3053. https://doi.org/10.1002/ejic.202100274 (2021).
40. Boulard, E. et al. Ferrous iron under oxygen-rich conditions in the deep mantle. *Geophys. Res. Lett.* **46**, 1348–1356. https://doi.org/10.1029/2019GL081922 (2019).
41. Wilke, M., Farges, F., Petit, P. E., Brown, G. E. & Martin, F. Oxidation state and coordination of Fe in minerals: An Fe K-XANES spectroscopic study. *Am. Mineral.* **86**, 714–730 (2001).
42. Carvalho-e-Silva, M. L. et al. Incorporation of Ni into natural goethite: An investigation by X-ray absorption spectroscopy. *Am. Mineral.* **88**, 876–882 (2003).
43. Beale, A. M. et al. Combined experimental and computational modelling studies of the solubility of nickel in strontium titanate. *J. Mater. Chem.* **19**, 4391–4400. https://doi.org/10.1039/B902591J (2009).
44. Gleason, A. E., Jeanloz, R. & Kunz, M. Pressure-temperature stability studies of FeOOH using X-ray diffraction. *Am. Mineral.* **93**, 1882–1885. https://doi.org/10.2138/am.2008.2942 (2008).
45. Otte, K., Pentcheva, R., Schmahl, W. & Rustad, J. Pressure-induced structural and electronic transitions in FeOOH from first principles. *Phys. Rev. B* **80**, 205116. https://doi.org/10.1103/PhysRevB.80.205116 (2009).

46. Suzuki, A. High-pressure X-ray diffraction study of ε-FeOOH. *Phys. Chem. Miner.* **37**, 153–157. https://doi.org/10.1007/s00269-009-0319-x (2010).
47. Bykova, E. et al. Structural complexity of simple Fe_2O_3 at high pressures and temperatures. *Nat. Commun.* **7**, 10661. https://doi.org/10.1038/ncomms10661 (2016).
48. Mao, H. K. et al. When water meets iron at Earth's core-mantle boundary. *Natl. Sci. Rev.* **4**, 870–878 (2017).
49. Hu, Q. et al. Mineralogy of the deep lower mantle in the presence of H2O. *Natl. Sci. Rev.* (4), nwaa098. https://doi.org/10.1093/nsr/nwaa098 (2020).
50. Harris, J. W. The recognition of diamond inclusions. Part 1: Syngenetic mineral inclusions. *Ind. Diam. Rev.* **28**, 402–410 (1968a).
51. Harris, J. W. The recognition of diamond inclusions. Part 2: Epigenetic mineral inclusions. *Ind. Diam. Rev.* **28**, 558–561 (1968b).
52. Stachel, T., Aulbach, S. & Harris, J. W. Mineral inclusions in lithospheric diamonds. *Rev. Mineral. Geochem.* **88**(1), 307–392. https://doi.org/10.2138/rmg.2022.88.06 (2022).
53. Wenz, M. D. et al. Fast identification of mineral inclusions in diamond at GSECARS using synchrotron X-ray microtomography, radiography and diffraction. *J. Synchrotron Rad.* **26**, 1–12 (2019).
54. Komabayashi, T., Omori, S. & Maruyama, S. Petrogenetic grid in the system MgO-SiO2-H2O up to 30 GPa, 1600°C: Applications to hydrous peridotite subducting into the Earth's deep interior. *J. Geophys. Res.* **109**, B03206. https://doi.org/10.1029/2003JB002651 (2004).
55. Maeda, F. et al. Diamond formation in the deep lower mantle: A high-pressure reaction of MgCO3 and SiO2. *Sci. Rep.* **7**, 40602. https://doi.org/10.1038/srep40602 (2017).
56. Nestola, F. et al. Extreme redox variations in a superdeep diamond from a subducted slab. *Nature* **613**, 85–89. https://doi.org/10.1038/s41586-022-05392-8 (2023).
57. Katsura, T., Yoneda, A., Yamazaki, D., Yoshino, T. & Ito, E. Adiabatic temperature profile in the mantle. *Phys. Earth Planet. Inter.* **183** (1), 212–218 (2010).
58. Walter, M. J. et al. Deep mantle cycling of Oceanic Crust: Evidence from Diamonds and Their Mineral Inclusions. *Science* **334**, 54–57. https://doi.org/10.1126/science.1209300 (2011).
59. Smith, E. M. et al. Large gem diamonds from metallic liquid in Earth's deep mantle. *Science* **354**, 1403–1405. https://doi.org/10.1126/science.aal1303 (2016).
60. Timmerman, S. et al. Primordial and recycled helium isotope signatures in the mantle transition zone. *Science* **365**, 692–694. https://doi.org/10.1126/science.aax5293 (2019).
61. Frost, D. J. & Myhill, R. Chemistry of the lower mantle. In Deep Earth: Physics and Chemistry of the Lower Mantle and Core (eds. Terasaki, H. & Fischer, R. A.) Geophysical Monograph Series, Ch. 18. https://doi.org/10.1002/9781118992487.ch18 (Wiley, 2016).
62. Tackley, P. et al. Effects of an endothermic phase transition at 670 km depth in a spherical model of convection in the Earth's mantle. *Nature* **361**, 699–704. https://doi.org/10.1038/361699a0 (1993).
63. Solheim, L. P. & Peltier, W. R. Avalanche effects in phase transition modulated thermal convection: A model of Earth's mantle. *J. Geophys. Res.* **99**, 6997–7018 (1994).
64. Gaherty, J. B. & Hager, B. H. Compositional vs. thermal buoyancy and the evolution of subducted lithosphere. *Geophys. Res. Lett.* **21**, 141–144 (1994).
65. Li, C. & Van Der Hilst, R. D. Structure of the upper mantle and transition zone beneath Southeast Asia from travel time tomography. *Journal of Geophysical Research: Solid Earth* **115**, B07308 (2010).
66. Myhill, R. Slab buckling and its effect on the distributions and focal mechanisms of deep-focus earthquakes. *Geophys. J. Int.* **192**, 837–853 (2013).
67. Frost, D. J. & McCammon, C. A. The redox state of Earth's mantle. *Annu. Rev. Earth Planet. Sci.* **36**, 389–420 (2008).
70. Howell, D. et al. μ-FTIR mapping: Distribution of impurities in different types of diamond growth. *Diamond Relat. Mater.* **29**, 29–36. https://doi.org/10.1016/j.diamond.2012.06.003 (2012).
71. Howell, D. et al. Platelet development in cuboid diamonds: Insights from micro-FTIR mapping. *Contrib. Mineral. Petrol.* **164**, 1011–1025 (2012).
72. Archilha, N. L. et al. MOGNO, the nano and microtomography beamline at Sirius, the Brazilian synchrotron light source. *J. Phys: Conf. Ser.* 14th International Conference on Synchrotron Radiation Instrumentation **2740**, 012033. https://doi.org/10.1088/1742-6596/2740/1/012033 (2023).
73. Miqueles, E. X., Martinez, G. Jr. & Guerrero, P. P. Fast image reconstruction at a synchrotron laboratory. In Proceedings of the 2020 SIAM Conference on Parallel Processing for Scientific Computing (PP20). Society for Industrial and Applied Mathematics https://doi.org/10.1137/1.9781611976137.49 (2020).
74. Dos Reis, R. D. et al. N.M. Preliminary overview of the Extreme Condition Beamline (EMA) at the new Brazilian Synchrotron Source (Sirius). Journal of Physics: Conference Series, 27th AIRAPT International Conference on High Pressure Science and Technology **1600**, 012003 https://doi.org/10.1088/1742-6596/1600/1/012003 (2020).
75. Prescher, C. & Prakapenka, V. B. DIOPTAS: A program for reduction of two-dimensional X-ray diffraction data and data exploration. *J. Appl. Crystallogr.* **48**, 223–230. https://doi.org/10.1107/S1600576715004306 (2015).
76. Tolentino, H. C. N. et al. The CARNAÚBA X-ray nanospectroscopy beamline at the Sirius-LNLS synchrotron light source: Developments, commissioning, and first science at the TARUMÃ station. J. Elect. Spect. Rela. Phen. **266**, 147339 https://doi.org/10.1016/j.elspec.2023.147339 (2023).
77. Camarda, C. M. et al. N. Nano X-ray Tomography at the CARNAÚBA Beamline (SIRIUS-LNLS) in diamond mineral inclusions. J. Phys.: Conf. Ser. 3010, 15th Int. Conf. on Synchrotron Radiation Instrumentation (SRI 2024), Hamburg, Germany. https://doi.org/10.1088/1742-6596/3010/1/012178 (2024).
78. Giannozzi, P. et al. QUANTUM ESPRESSO: A modular and open-source software project for quantum simulations of materials. *J. Phys.: Condens. Matter* **21**, 395502. https://doi.org/10.1088/0953-8984/21/39/395502 (2009).
79. Giannozzi, P. et al. Advanced capabilities for materials modelling with Quantum ESPRESSO. *J. Phys.: Condens. Matter* **29**, 465901. https://doi.org/10.1088/1361-648X/aa8f79 (2017).
80. Prandini, G. et al. Precision and efficiency in solid-state pseudopotential calculations. *NPJ Comput. Mater.* **4**, 72. https://doi.org/10.1038/s41524-018-0127-2 (2018).
81. Perdew, J. P., Burke, K. & Ernzerhof, M. Generalized gradient approximation made simple. *Phys. Rev. Lett.* **77**, 3865–3868. https://doi.org/10.1103/PhysRevLett.77.3865 (1996).
82. Bunău, O. & Joly, Y. Self-consistent aspects of x-ray absorption calculations. *J. Phys.: Condens. Matter* **21**, 345501. https://doi.org/10.1088/0953-8984/21/34/345501 (2009).
83. Guda, S. A. et al. Optimized finite difference method for the full-potential XANES simulations: Application to molecular adsorption geometries in MOFs and metal–ligand intersystem crossing transients. *J. Chem. Theory Comput.* **11**, 4512–4521. https://doi.org/10.1021/acs.jctc.5b00327 (2015).
84. Bourke, J. D., Chantler, C. T. & Joly, Y. FDMX: Extended X-ray absorption fine structure calculations using the finite difference method. *J. Synchrotron Radiat.* **23**, 551–559. https://doi.org/10.1107/S1600577516001193 (2016).

Author contributions

Conceptualization: CMC, FG, TJ, SWS, DGCMethodology- Experiments realization: CMC, FMCS, HCNT, FG, DGC, NLAMethodology- Data process: CMC, FMCS, HCNT, IT, PF, ME, JFGAO, NLA, JMAFunding acquisi-

tion: FG, TJ, RFSupervision: FG, TJ, HCNTWriting – original draft: CMC, FGWriting – review & editing: CMC, FG, FMCS, DGC, TJ, JMA, SWS, HCNT, PF, ME, JFGAO, IT, RF, NLA.

Declarations

Competing interests
The authors declare no competing interests.

Additional information
Supplementary Information The online version contains supplementary material available at https://doi.org/10.1038/s41598-026-46683-8.

Correspondence and requests for materials should be addressed to F.G.

Reprints and permissions information is available at www.nature.com/reprints.

Publisher's note Springer Nature remains neutral with regard to jurisdictional claims in published maps and institutional affiliations.